# Supporting Information

## Bridging Quantum Mechanics to Organic Liquid Properties via a Universal Force Field

Tianze Zheng,* Xingyuan Xu, Zhi Wang, Zhenze Yang, Yuanheng Wang, Xu Han, Zhenliang Mu, Ziqing Zhang, Siyuan Liu, Sheng Gong, Kuang Yu, and Wen Yan*

*ByteDance Seed*

E-mail: zhengtianze@bytedance.com; wen.yan@bytedance.com

## Supporting Figures

# Supporting Tables

# 1 Molecule Abbreviations

Here, we list all the molecule abbreviations involved in this paper.

Table S1: Molecule abbreviations.

| Abbreviation | Name | SMILES |
|---|---|---|
| EC | Ethylene carbonate | C1COC(=O)O1 |
| DMC | Dimethyl carbonate | COC(=O)OC |
| EMC | Ethyl methyl carbonate | CCOC(=O)OC |
| AN | Acetonitrile | CC#N |
| MA | Methyl acetate | CC(=O)OC |
| PC | Propylene carbonate | CC1COC(=O)O1 |
| TFP | Tris(2,2,2-trifluoroethyl) phosphate | O=P(OCC(F)(F)F)(OCC(F)(F)F)OCC(F)(F)F |
| TGDME | Triethylene glycol dimethyl ether | COCCOCCOCCOC |
| EMP | 1-methoxy-3-trifluoethoxypropane | COCCCOCC |
| F3EMP | 1-Methoxy-3-(2,2,2-trifluoroethoxy)propane | COCCCOCC(F)(F)F |
| EA | Ethyl acetate | CCOC(=O)C |
| GBL | Gamma-butyrolactone | C1CC(=O)OC1 |
| FEMC | Methyl 2,2,2-trifluoroethyl carbonate | COC(=O)OCC(F)(F)F |
| FEC | Fluoroethylene carbonate | C1C(OC(=O)O1)F |
| DFEC | Di-fluoro ethylene carbonate | O1[C@H](F)[C@@H](F)OC1=O |
| TFPC | 4-(trifluoromethyl)-1,3-dioxolan-2-one | C1C(OC(=O)O1)C(F)(F)F |
| LiPF6 | Lithium hexafluorophosphate | [Li+].F[P-](F)(F)(F)(F)F |
| LiFSI | Lithium bis(fluorosulfonyl)imide | [Li+].O=S(=O)(F)[N-]S(=O)(=O)F |
| LiTFSI | Lithium bis(trifluoromethanesulfonyl)imide | O=S(=O)([N-]S(=O)(=O)C(F)(F)F)C(F)(F)F |
| Ani | Aniline | Nc1ccccc1 |
| NOM | Nitromethane | C[N+](=O)[O-] |
| HAC | Acetic acid | CC(=O)O |
| BZ | Benzene | c1ccccc1 |
| ACE | Acetone | CC(C)=O |
| EtCl | Ethyl chloride | CCCl |
| EtSH | Ethanethiol | CCS |

## 2 Cluster Geometries

The cluster components and geometries involved in Figure 2 (e) and (f) are shown here. The cluster's geometries were first optimized with DFT at the B3LYP-D3(BJ)/def2-SVPD level, represented by the light blue carbon atoms. The conformations were then re-optimized using ByteFF-Pol, represented by the grey carbon atoms. During the force field optimization, the atomic positions were restrained with a weak harmonic force (1 kcal/mol/Å$^2$) to ensure the system remained in the same local minimum. DFT results are marked by light blue carbons and ByteFF-Pol results are marked by grey carbons. The cluster geometries are visualized using Maestro.[4]

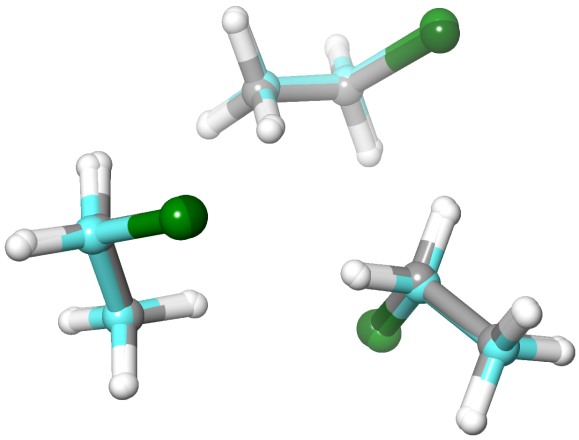

Figure S1: **Geometry of cluster-n1.** The cluster contains three EtCl molecules.

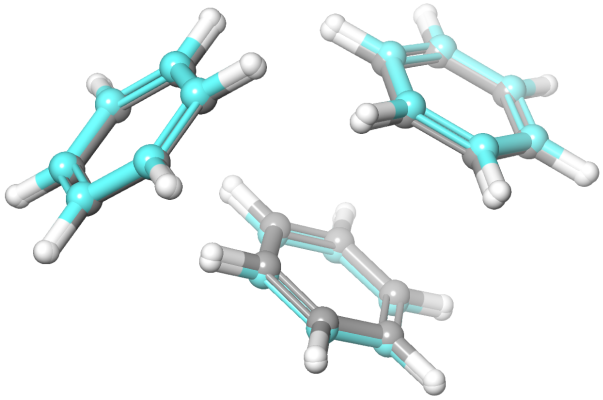

Figure S2: **Geometry of cluster-n2.** The cluster contains three BZ molecules.

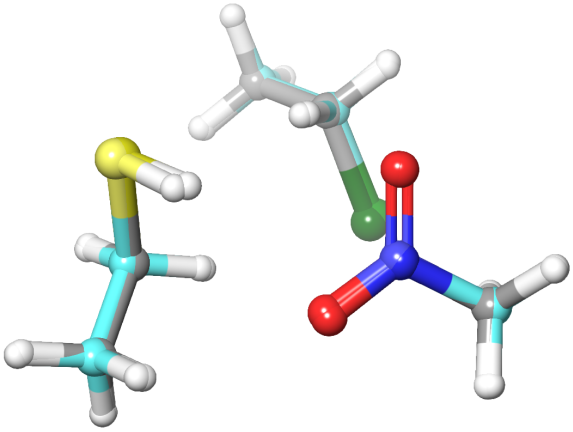

Figure S3: **Geometry of cluster-n3.** The cluster contains one NOM, one EtCl and one EtSH molecule.

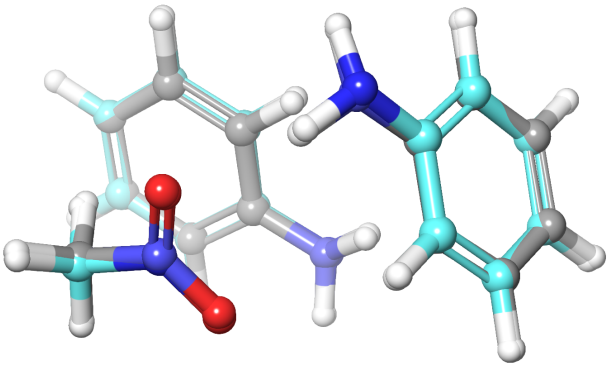

Figure S4: **Geometry of cluster-n4.** The cluster contains two Ani and one NOM molecule.

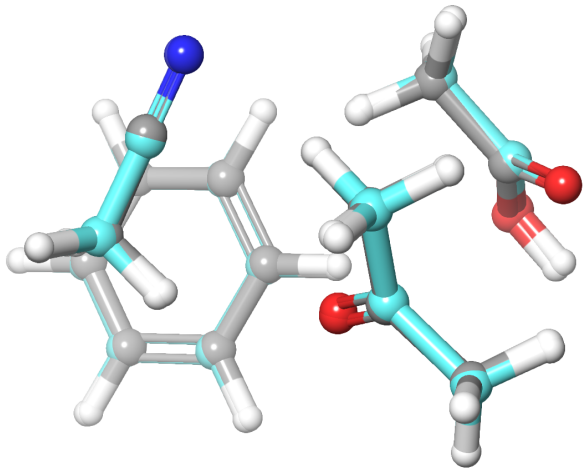

Figure S5: **Geometry of cluster-n5.** The cluster contains one HAC, one BZ, one AN and one ACE molecule.

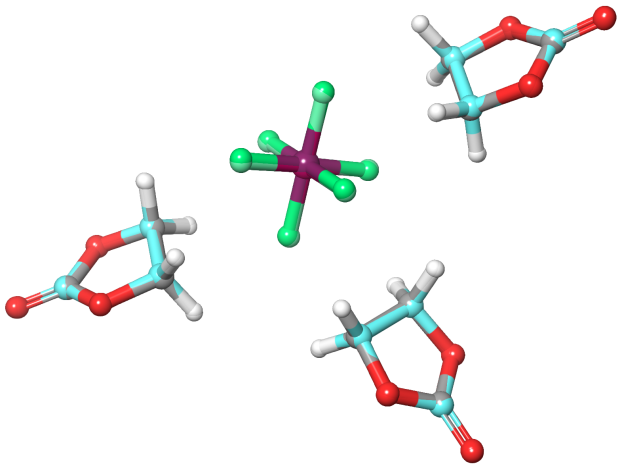

Figure S6: **Geometry of cluster-i1.** The cluster contains three EC and one $PF6^-$ anion.

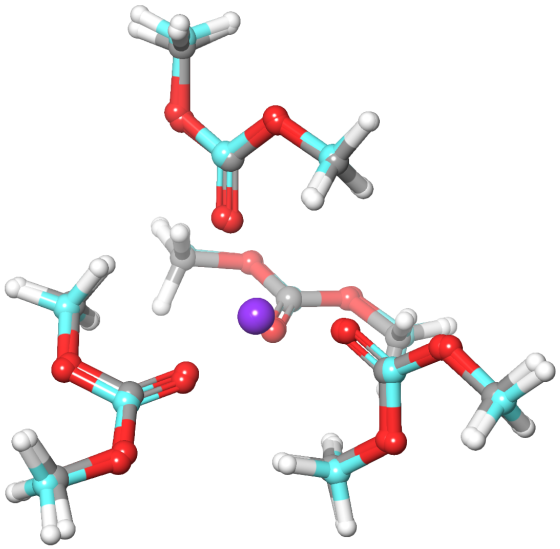

Figure S7: **Geometry of cluster-i2.** The cluster contains four DMC and one $Li^+$ cation.

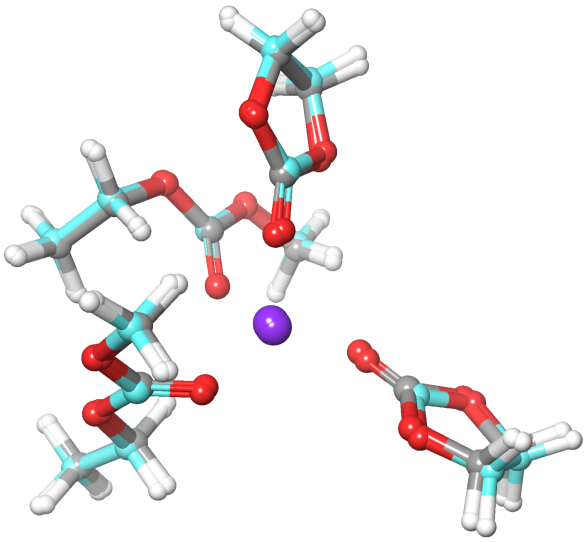

Figure S8: **Geometry of cluster-i3.** The cluster contains two EMC, two EC and one $Li^+$ cation.

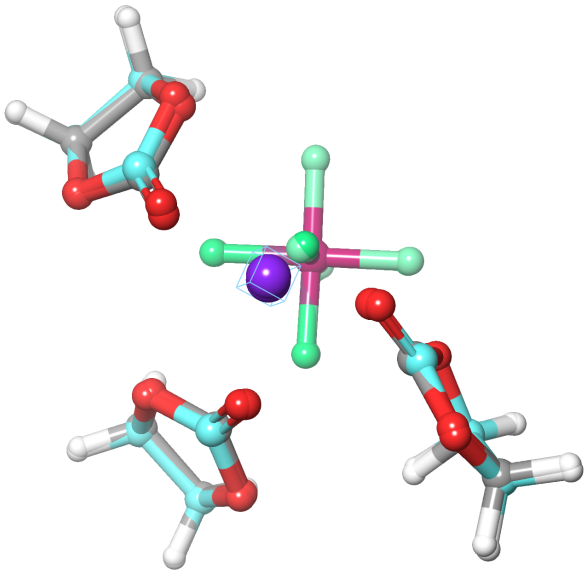

Figure S9: **Geometry of cluster-i4.** The cluster contains three EC, one $Li^+$ cation and one $PF6^-$ anion.

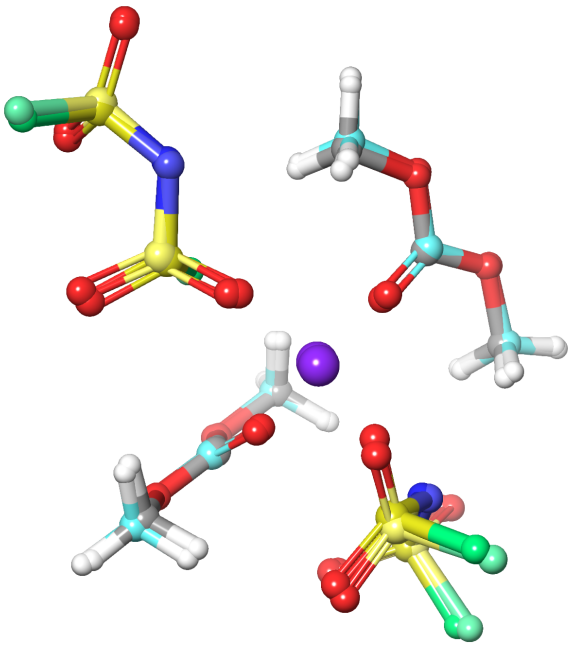

Figure S10: **Geometry of cluster-i5.** The cluster contains two DMC, one $Li^+$ cation and two $FSI^-$ anions.

# 3 Measurement of Similarity

Given a molecule, we calculate its similarity to a reference set of molecules through an atomic environment-derived algorithm. We first define the similarity between two atoms as:

$$S_{ij} = \cos(\theta_{ij}) = \frac{||\boldsymbol{h}_i \cdot \boldsymbol{h}_j||}{||\boldsymbol{h}_i|| \cdot ||\boldsymbol{h}_j||}, \tag{S1}$$

where $\boldsymbol{h}_i$ and $\boldsymbol{h}_j$ are the hidden representation of atoms $i$ and $j$, produced by the ByteFF-Pol GNN model.

Next, we determine an atom's similarity to a reference set of molecules, $\mathcal{J}$. This score, $S_i(\mathcal{J})$, is the average of the top $k$ highest similarity values between atom i and all atoms of the same element within the reference set:

$$S_i(\mathcal{J}) = \frac{1}{k} \sum \mathrm{Top}k_j\{S_{ij} | j \in \mathcal{J}_i\}. \tag{S2}$$

The set $\mathcal{J}_i$ contains all atoms in the reference set $\mathcal{J}$ with the same element as $i$. For our calculations, we use $k = 5$. The usage of Top $k$ values helps to obtain a robust and comprehensive similarity measurement.

Finally, the similarity of an entire molecule $M$ to the reference set $\mathcal{J}$, $S_M(\mathcal{J})$, is calculated as the minimum similarity of each atom in the molecule:

$$S_M(\mathcal{J}) = \min_{i \in M} S_i(\mathcal{J}). \tag{S3}$$

The choice of the minimum value ensures that the similarity measurement is sensitive to the "out-of-distribution" (OOD) atomic environment.

# 4 Dataset Details

To train ByteFF-Pol, we curate a large-scale, high-accuracy dataset consisting molecular dimer references obtained from the absolutely localized molecular orbital energy decomposition analysis (ALMO-EDA). Our initial molecule set comprises 315 neutral molecules and 4 ions. The neutral molecules include those selected from the NIST ThermoML archive[5] and common solvent molecules used in electrolytes from literatures.[6] The ions include $Li^+$, $PF_6^-$, $FSI^-$, $TFSI^-$, derived from typical lithium salts employed in electrolytes. These molecules were combined pairwise to form 51040 molecular dimers.

To further expand the chemical space coverage of our dataset, we incorporated additional molecules from the CRC Handbook.[7] These molecules were filtered based on their similarity to the initial molecular set, calculated as described above. Subsequently, 75 new molecules were selected and paired both among themselves and with 92 representative molecules from the initial set. In total, 60,790 distinct molecular dimers were assembled from 394 molecules (including 4 ions).

Next, we sampled 100 conformations for each dimer. Starting from the initial conformation generated by RDKit, the conformation of each molecule was optimized independently using the geomeTRIC optimizer[8] at the B3LYP-D3(BJ)/DZVP level of theory. Each pair of optimized molecules was then combined with a random orientation and their separation distance uniformly sampled in the range of 1.5 to 10.0 Å. Additionally, Gaussian noise with a standard deviation of 0.05 Å was added to the atomic coordinates to perturb the molecular conformations.

Finally, these samples were labeled via quantum mechanical (QM) calculations. Specifically, the second-generation ALMO-EDA calculations at the $\omega$B97M-V/def2-TZVPD level were performed to derive decomposed interaction energy labels. The $\omega$B97M-V/def2-TZVPD level of theory was selected for its proven to be both efficient and accurate, especially for intermolecular interaction.

In summary, our training dataset comprises approximately 6 million conformations with

ALMO-EDA labels, assembled from nearly 400 distinct molecules. Among these, 5.4 million samples were allocated for training and 0.6 million for validation.

For the benchmark datasets, a series of filtering and cleaning steps were performed. ByteFF-Pol currently supports nine elements, including C, H, O, N, P, S, F, Cl, and Li; thus, molecules containing other elements were excluded from the benchmark datasets. Additionally, since molecular dynamics (MD) simulations of systems near the boiling or freezing points can be problematic, data points measured at temperatures close to these critical points were also excluded from the benchmark datasets. We are extending the element coverage of our training dataset to enhance the power of ByteFF-Pol.

# 5 Theory and Implementation of Second-Generation ALMO-EDA

Our EDA training data is computed with Q-Chem[9] version 6.1. We also reproduce the EDA algorithm in GPU4PySCF, available in version 1.4.2.

In this section we provide a detailed description on the second-generation ALMO-EDA, and how each term is implemented in GPU4PySCF:

As mentioned in the main text, the total intermolecular interaction energy $U_{\text{int}}^{\text{DFT}}$ is defined as the difference between the fully-relaxed cluster SCF energy $U^{\text{DFT}}[D_{\text{full}}]$ and the sum of individual isolated fragment SCF energy $U_F^{\text{DFT}}[D_F]$:

$$U_{\text{int}}^{\text{DFT}} = U^{\text{DFT}}[D_{\text{full}}] - \sum_F U_F^{\text{DFT}}[D_F] \tag{S4}$$

In the second-generation ALMO-EDA, the total intermolecular interaction energy of a cluster is first decomposed into frozen, polarization, and charge transfer terms:[10]

$$U_{\text{int}}^{\text{DFT}} = U_{\text{frz}}^{\text{EDA}} + U_{\text{pol}}^{\text{EDA}} + U_{\text{ct}}^{\text{EDA}} \tag{S5}$$

and the frozen term is further decomposed into dispersion, electrostatic, and Pauli terms:[11]

$$U_{\text{frz}}^{\text{EDA}} = U_{\text{disp}}^{\text{EDA}} + U_{\text{est}}^{\text{EDA}} + U_{\text{pauli}}^{\text{EDA}} \tag{S6}$$

The frozen energy $U_{\text{frz}}^{\text{EDA}}$ describes the intermolecular interaction energy without any molecular orbital relaxation. It is defined as the difference between the cluster energy evaluated at the frozen density matrix $D_{\text{frz}}$ and the sum of individual isolated fragment SCF energy $U_F^{\text{DFT}}[D_F]$:

$$U_{\text{frz}}^{\text{EDA}} = U^{\text{DFT}}[D_{\text{frz}}] - \sum_F U_F^{\text{DFT}}[D_F] \tag{S7}$$

where the frozen density matrix is the cluster-size-idempotent density constructed from unrelaxed fragment molecular orbitals (MOs):[12]

$$D_{\mathrm{frz}} = C_{\mathrm{frz}}^{\mathrm{occ}} \left( (C_{\mathrm{frz}}^{\mathrm{occ}})^T S C_{\mathrm{frz}}^{\mathrm{occ}} \right)^{-1} (C_{\mathrm{frz}}^{\mathrm{occ}})^T \tag{S8}$$

where $C_{\mathrm{frz}}^{\mathrm{occ}}$ is a block diagonal matrix where each diagonal block is the occupied part of each isolated fragment MO coefficients, and $S$ is the overlap matrix of the cluster.

The electrostatic energy $U_{\mathrm{est}}^{\mathrm{EDA}}$ is defined as the sum of Coulomb interactions between total charge densities of each pair of fragments:

$$U_{\mathrm{est}}^{\mathrm{EDA}} = \sum_{A<B}^{n_{\mathrm{frag}}} \int dr_1 \int dr_2 \; \tilde{\rho}_A^{\mathrm{tot}}(r_1) \frac{1}{r_{12}} \tilde{\rho}_B^{\mathrm{tot}}(r_2) \tag{S9}$$

where the total charge density of each fragment includes the electron density as well as the nuclear density:

$$\tilde{\rho}_F^{\mathrm{tot}}(r) = \sum_{\mu\nu}^{n_{AO}^{\mathrm{cluster}}} \tilde{D}_{\mu\nu}^F \mu(r)\nu(r) + \sum_{\mathrm{nuc}}^{n_{\mathrm{nuc}}^F} q_{\mathrm{nuc}}^F \delta(r - R_{\mathrm{nuc}}^F) \tag{S10}$$

The density matrix of each fragment $\tilde{D}^F$ has the dimension of the number of atomic orbitals (AOs) of the whole cluster, and is obtained via optimization of the kinetic energy pressure:[11]

$$U_{\mathrm{KEP}} = \sum_{F}^{n_{\mathrm{frag}}} U_F^{\mathrm{DFT}}[\tilde{D}^F] - U_F^{\mathrm{DFT}}[D^F] \tag{S11}$$

under the constraint that only the MO rotation within all occupied space of each fragment MO is allowed. $D^F$ is the unrelaxed cluster-size-idempotent density of each fragment, constructed in a similar manner as Eq. S8, and also serves as the initial guess for $\tilde{D}^F$ optimization. The detail of this constrained optimization process can be found at Ref 11, we adopt the same second-order algorithm with the same form of approximated Hessian.

An alternative definition of the electrostatic energy, usually referred to as the "classical

electrostatic energy", is defined as

$$U_{\text{cls-est}}^{\text{EDA}} = \sum_{A<B}^{n_{\text{frag}}} \int dr_1 \int dr_2 \; \rho_A^{\text{tot}}(r_1) \frac{1}{r_{12}} \rho_B^{\text{tot}}(r_2) \tag{S12}$$

It is similar to the electrostatic energy, except that the density is not optimized for kinetic energy pressure ($D^F$ is used to evaluated $\rho_F^{\text{tot}}$, instead of $\tilde{D}^F$ evaluating $\tilde{\rho}_F^{\text{tot}}$). This term is computed but never used.

The dispersion energy $U_{\text{disp}}$ is defined as the difference between the interfragment exchange-correlation (XC) interaction of the desired DFT functional, and that of a "dispersion-free (DF)" functional:[11]

$$U_{\text{disp}}^{\text{EDA}} = \left( U_{XC}[D_{\text{frz}}] - \sum_{F}^{n_{\text{frag}}} U_{XC}[\tilde{D}^F] \right) - \left( U_{XC}^{DF}[D_{\text{frz}}] - \sum_{F}^{n_{\text{frag}}} U_{XC}^{DF}[\tilde{D}^F] \right) \tag{S13}$$

Following Ref 11, Hartree-Fock exchange is chosen as the dispersion-free functional.

The Pauli energy $U_{\text{pauli}}^{\text{EDA}}$ describes the volume exclusion effect between the electron densities of different fragments. It is obtained as the remainder of the frozen energy:[13]

$$U_{\text{pauli}}^{\text{EDA}} = U_{\text{frz}}^{\text{EDA}} - U_{\text{est}}^{\text{EDA}} - U_{\text{disp}}^{\text{EDA}} \tag{S14}$$

Since the electrostatic and Pauli terms become singular but opposite when the fragments come close to each other, we combine them and define:

$$U_{\text{est\_pauli}}^{\text{EDA}} = U_{\text{est}}^{\text{EDA}} + U_{\text{pauli}}^{\text{EDA}} = U_{\text{frz}}^{\text{EDA}} - U_{\text{disp}}^{\text{EDA}} \tag{S15}$$

This combined term is also referred to as the dispersion-free frozen energy.[14] Instead of the electrostatic and Pauli energies, only $U_{\text{est\_pauli}}^{\text{EDA}}$ is included in the training data.

The polarization energy $U_{\text{pol}}$ is obtained via another constraint optimization: The cluster energy is optimized under the constraint that only the MO rotation within the fragment

electric-field response function (FERF) with dipolar and quadrupolar response (DQ) subspace of each fragment is allowed. FERF-DQ space is the minimal variational space necessary to relax its orbital when a weak external electric field or field gradient is applied. This constrained relaxation permits only the polarization response of each fragment in the present of other fragments, and the resulting polarized density matrix $D_{\mathrm{pol}}$ defines the polarization energy:

$$U_{\mathrm{pol}}^{\mathrm{EDA}} = U^{\mathrm{DFT}}[D_{\mathrm{pol}}] - U_{\mathrm{frz}}^{\mathrm{EDA}} \tag{S16}$$

The definition of FERF-DQ subspace can be found in Ref 15, however, we restate it here to address some potential ambiguities.

The FERF-DQ subspace of a fragment describes the occupied and virtual MO subspace necessary to response to an applied weak uniform electric field or field gradient. It is obtained by solving the coupled-perturbed (CP) SCF equation:

$$\sum_{b}^{n_{\mathrm{vir}}} \sum_{j}^{n_{\mathrm{occ}}} H_{ai,bj} \kappa_{bj}^{\mathrm{pole}} = -2M_{ai}^{\mathrm{pole}} \tag{S17}$$

where $H$ is the SCF orbital Hessian, $\kappa^{\mathrm{pole}}$ is the first order orbital rotation matrix, and $M^{\mathrm{pole}}$ is one multipole moment matrix in MO space. We adopt the convention to index occupied MO with $i, j, ...$, virtual MO with $a, b, ...$, and AO with $\mu, \nu, ....$ Since the response to electric field is required, we need to construct the three dipole moment matrices along three spatial dimension $\alpha = x, y, z$:

$$M_{\mu\nu}^{\mathrm{dip},\alpha} = (\mu | r_\alpha - R_\alpha | \nu) \tag{S18}$$

The origin $R$ is chosen as the center of mass of each fragment. Since the response to electric field gradient is also required, we need to construct the six traceless Cartesian quadrupole

moment matrices:

$$M_{\mu\nu}^{\mathrm{quad},\alpha\beta} = \frac{3}{2}(\mu|(r_\alpha - R_\alpha)(r_\beta - R_\beta)|\nu) - \frac{1}{2}\delta_{\alpha,\beta}\sum_{\gamma=x,y,z}(\mu|(r_\gamma - R_\gamma)^2|\nu) \tag{S19}$$

and extract the five spherical quadrupole moment matrices:

$$\begin{aligned}
M^{\mathrm{quad},2,-2} &= \frac{2}{\sqrt{3}}M^{\mathrm{quad},xy} \\
M^{\mathrm{quad},2,-1} &= \frac{2}{\sqrt{3}}M^{\mathrm{quad},yz} \\
M^{\mathrm{quad},2,0} &= M^{\mathrm{quad},zz} \\
M^{\mathrm{quad},2,1} &= \frac{2}{\sqrt{3}}M^{\mathrm{quad},xz} \\
M^{\mathrm{quad},2,2} &= \frac{1}{\sqrt{3}}(M^{\mathrm{quad},xx} - M^{\mathrm{quad},yy})
\end{aligned} \tag{S20}$$

For FERF-DQ, there are eight moment matrices and thus eight CPSCF to solve. The CPSCF is solved exactly in our implementation, however an approximate orbital Hessian also turns out to provide reasonable polarization energy.[16] Then for each of the eight resulting $\kappa^{\mathrm{pole}}$ matrices, a singular value decomposition (SVD) is performed:

$$\kappa^{\mathrm{pole}} = L^{\mathrm{pole}}\Sigma^{\mathrm{pole}}(R^{\mathrm{pole}})^T \tag{S21}$$

Thera are at most $n_{\mathrm{occ}}$ left singular vector in $L^{\mathrm{pole}}$ (of size $n_{\mathrm{vir}} \times n_{\mathrm{vir}}$) associated with a non-zero singular value, and other left singular vectors are discarded. The FERF virtual space for this field response is

$$V_{\mu a}^{\mathrm{pole}} = \sum_{b}^{n_{\mathrm{vir}}} C_{\mu b}^{\mathrm{vir}} L_{ba}^{\mathrm{pole}} \tag{S22}$$

The index $a$ depends on the number of non-zero singular value of $\kappa^{\mathrm{pole}}$. After all eight $V^{\mathrm{pole}}$ matrices are obtained, they are concatenated, and also concatenated with the occupied space

of MO, to form a FERF-DQ space matrix:

$$C^{\mathrm{FERF-DQ}} = \begin{pmatrix} C^{\mathrm{occ}} & V^{\mathrm{dip},x} & V^{\mathrm{dip},y} & V^{\mathrm{dip},z} & V^{\mathrm{quad},2,-2} & V^{\mathrm{quad},2,-1} & V^{\mathrm{quad},2,0} & V^{\mathrm{quad},2,1} & V^{\mathrm{quad},2,2} \end{pmatrix} \tag{S23}$$

The dimension of $C^{\mathrm{FERF-DQ}}$ is $n_{AO} \times n_{\mathrm{FERF-DQ}}$, where $n_{\mathrm{FERF-DQ}}$ is system dependent but not greater than $9n_{\mathrm{occ}}$. Another SVD is performed on $C^{\mathrm{FERF-DQ}}$:

$$C^{\mathrm{FERF-DQ}} = L^{\mathrm{FERF-DQ}} \Sigma^{\mathrm{FERF-DQ}} (R^{\mathrm{FERF-DQ}})^T \tag{S24}$$

and the FERF-DQ subspace projector is obtained as the left singular vectors $L^{\mathrm{FERF-DQ}}$ associated with non-zero singular values. One subtle point remains here about the threshold for non-zero singular values in the nine SVD procedures. Unfortunately the polarization energy is sensitive to the choice of this threshold, as when a "wrong" virtual space component is included, an error as large as 1 kJ/mol has been observed, and rotational invariance is broken. The situation became more difficult as some anions, $PF_6^-$ for example, have a relatively continuous spectrum of singular values, and the boundary between zero and non-zero values are blurry. With some preliminary experiments, we set our threshold to $10^{-4}$, regardless of the fragment size or composition.

Once the FERF-DQ subspace projector for each fragment is obtained, we construct the cluster projector ($G$ in Ref 15) as a block diagonal matrix where each diagonal block is the projector of each fragment. The detail of the following constrained optimization process can be found at Ref 15, we adopt the non-orthogonal fragment subspace (i.e. $G$ never changes from the form above), the Stoll approach to apply the projection, and a first-order direct inversion of iterative subspace (DIIS) algorithm for SCF. As a result of the constrained optimization, a polarized density matrix $D_{\mathrm{pol}}$ is obtained, and the polarization energy is obtained using Eq. S16.

The charge transfer energy $U_{\mathrm{ct}}^{\mathrm{EDA}}$ is associated with further orbital relaxation involving

intermolecular orbital mixing, in another word, electron density flowing between fragments. It is obtained as the remainder of the total EDA energy:[13]

$$U_{\mathrm{ct}}^{\mathrm{EDA}} = U_{\mathrm{int}}^{\mathrm{DFT}} - U_{\mathrm{frz}}^{\mathrm{EDA}} - U_{\mathrm{pol}}^{\mathrm{EDA}} \tag{S25}$$

# 6 Model Polarization in Force Field

The polarization energy is the most complex part of the force field function. Similar with the AMOEBA force field,[17] the polarization effect is modeled using induced dipoles, $\boldsymbol{\mu}$. These dipoles are calculated by a polarizability parameters $\boldsymbol{\alpha}$ and the total electric field $\boldsymbol{E}^t$:

$$\boldsymbol{\mu} = \boldsymbol{\alpha}\boldsymbol{E}^t = \boldsymbol{\alpha}\left(\boldsymbol{E}^p + \boldsymbol{E}^\mu\right), \tag{S26}$$

where $\boldsymbol{E}^p$ is the electric field generated by permanent multipoles and $\boldsymbol{E}^\mu = -\boldsymbol{T}^\mu\boldsymbol{\mu}$ is the field arising from other induced dipoles. As discussed in the main article, we have simplified the permanent multipoles to only include the atomic charge $q$. By defining $\tilde{\boldsymbol{T}} = \boldsymbol{\alpha}^{-1} + \boldsymbol{T}^\mu$, the induced dipoles is the solution to the linear equation:

$$\tilde{\boldsymbol{T}}\boldsymbol{\mu} = \boldsymbol{E}^p \tag{S27}$$

In AMOEBA, this equation is solved iteratively, which is efficient for large MD systems. However, since the molecular dimers used in our training procedure are much smaller, we solve this equation by the direct inversion of $\tilde{\boldsymbol{T}}$.

A scaling factor, $s_{ij}$, is used to avoid unphysical polarization between chemically bonded atoms. The assignment scheme for this factor in the AMOEBA force field is quite complex. We've simplified this by aligning it with the charge scaling factor used by OPLS-AA, i.e. 0.0 for 1-2 and 1-3 connected atoms, 0.5 for 1-4 connected atoms, and 1.0 for 1-5 connected atoms or other atom pairs.

Besides, short-ranged polarization interactions are described using a Thole damping function to prevent polarization collapse at short distances.[18] The electron density is modeled as:

$$\rho = \frac{3a}{4\pi}\exp(-a\frac{r_{ij}^3}{\sqrt{\alpha_i\alpha_j}}). \tag{S28}$$

Here, $a$ is a constant dimensionless parameter that controls the strength of the damping, which is 0.39 for our model. $\alpha_i$ is polarizability which is predicted by the ByteFF-Pol GNN model.

Based on the Thole damping and scaling factor,

$$\boldsymbol{E}_i^p = \sum_j s_{ij} \cdot \lambda_3 \frac{q_j}{|\boldsymbol{r}_{ij}|^3} \boldsymbol{r}_{ij} \tag{S29}$$

$$\boldsymbol{T}_{ij}^{\mu} = s_{ij} \cdot \frac{3\lambda_5 \boldsymbol{r}_{ij} \otimes \boldsymbol{r}_{ij} - \lambda_3 |\boldsymbol{r}_{ij}|^2 I_{3\times 3}}{|\boldsymbol{r}_{ij}|^5} \tag{S30}$$

where $\lambda_3 = 1 - \exp(-a\frac{r_{ij}^3}{\alpha_{ij}}), \lambda_5 = 1 - (1 + a\frac{r_{ij}^3}{\alpha_{ij}}) \exp(\frac{r_{ij}^3}{\alpha_{ij}})$.

Substituting $\boldsymbol{E}_i^p$ and $\boldsymbol{T}_{ij}^{\mu}$ into Eq. S27, we can solve $\boldsymbol{\mu}$ and then get

$$U_{\text{pol}} = -\frac{1}{2} \sum_i \mu_i E_i^p. \tag{S31}$$

# 7 Training Procedures

Our training procedure include three stages: pre-training stage, training stage and fine-tuning stage. This three-stage training procedure can help the training process smoothly and self-consistently.

## 7.1 Pre-training Stage

In the first stage, we train the model to learn the local chemical environment and bonded parameters. As our previous job, ByteFF,[19] can predict bonded parameters with broad chemical space coverage with state-of-the-art accuracy, we train the ByteFF-Pol GNN model to reproduce the performance. Therefore, a mean squared error (MSE) loss is used to distill the bonded parameters from ByteFF model. Except bonded terms, the atomic charge and volume are fitted to the minimal basis iterative Stockholder (MBIS) results at the level of PBE0/def2-TZVPD. These values severed as excellent initial guess for ByteFF-Pol non-bonded parameters, and also helped the model to learning the atomic environment concerning the non-bonded interactions. The total loss is as follows,

$$\mathcal{L}_{\text{pretrain}} = w_{\text{bonded}}\mathcal{L}_{\text{MSE}}^{\text{bonded}} + w_{\text{charge}}\mathcal{L}_{\text{MSE}}^{\text{charge}} + w_{\text{volume}}\mathcal{L}_{\text{MSE}}^{\text{volume}}, \tag{S32}$$

where $w_{\text{bonded}}$ was set to 0.1, and $w_{\text{charge}}$ and $w_{\text{volume}}$ were set to 1.0.

## 7.2 Training Stage

In the second stage, the interaction energy predicted by the ByteFF-Pol is fitted to the ALMO-EDA labels. A critical aspect of training the force field using ALMO-EDA labels is ensuring that the decomposition of the force field interaction energy aligns consistently with the decomposition scheme employed in ALMO-EDA. The dispersion energy is separated

straightforwardly,

$$U_{\text{disp}}^{\text{FF,inter}} = U_{\text{disp}}^{\text{FF}}(r_{\text{full}}) - \sum_F U_{\text{disp}}^{\text{FF}}(r_F). \tag{S33}$$

$r_{\text{full}}$ and $r_F$ are the atomic coordinates of the full cluster and fragment $F$, respectively. The fitting target of $U_{\text{disp}}^{\text{FF,inter}}$ is $U_{\text{disp}}^{\text{EDA}}$ as defined in Eq. S13.

For the freeze energy, the polarization term should be calculated with the induced dipole derived for the isolated fragments ($\mu_F^{\text{ind}}$),

$$\begin{aligned} U_{\text{frz}}^{\text{FF,inter}} = &\left(U_{\text{rep}}^{\text{FF}}(r_{\text{full}}) + U_{\text{disp}}^{\text{FF}}(r_{\text{full}}) + U_{\text{est}}^{\text{FF}}(r_{\text{full}}) + U_{\text{pol}}^{\text{FF}}(r_{\text{full}}; \mu_F^{\text{ind}})\right) \\ &- \sum_F \left(U_{\text{rep}}^{\text{FF}}(r_F) + U_{\text{disp}}^{\text{FF}}(r_F) + U_{\text{est}}^{\text{FF}}(r_F) + U_{\text{pol}}^{\text{FF}}(r_F; \mu_F^{\text{ind}})\right). \end{aligned} \tag{S34}$$

By subtracting the dispersion component, the remaining energy is expressed as:

$$\begin{aligned} U_{\text{est\_rep}}^{\text{FF,inter}} &= U_{\text{frz}}^{\text{FF,inter}} - U_{\text{disp}}^{\text{FF,inter}} \\ &= \left(U_{\text{rep}}^{\text{FF}}(r_{\text{full}}) + U_{\text{est}}^{\text{FF}}(r_{\text{full}}) + U_{\text{pol}}^{\text{FF}}(r_{\text{full}}; \mu_F^{\text{ind}})\right) \\ &- \sum_F \left(U_{\text{rep}}^{\text{FF}}(r_F) + U_{\text{est}}^{\text{FF}}(r_F) + U_{\text{pol}}^{\text{FF}}(r_F; \mu_F^{\text{ind}})\right). \end{aligned} \tag{S35}$$

Since the repulsion part and the permutation electrostatic part are commonly cancel each other out, and there are multiple splitting schemes exist for these components, we directly fit $U_{\text{est\_rep}}^{\text{FF,inter}}$ to $U_{\text{est\_pauli}}^{\text{EDA}}$ as defined in Eq. S15.

Subsequently, the induced dipoles are relaxed to obtain $\mu_{\text{full}}^{\text{ind}}$. The polarization energy is the energy difference before and after relaxation:

$$U_{\text{pol}}^{\text{FF,inter}} = U_{\text{pol}}^{\text{FF}}(r_{\text{full}}; \mu_{\text{full}}^{\text{ind}}) - U_{\text{pol}}^{\text{FF}}(r_{\text{full}}; \mu_F^{\text{ind}}). \tag{S36}$$

The fitting target of $U_{\text{pol}}^{\text{FF,inter}}$ is $U_{\text{pol}}^{\text{EDA}}$ as defined in Eq. S16.

Finally, the charge transfer energy takes a relatively simple form:

$$U_{\mathrm{ct}}^{\mathrm{FF,inter}} = U_{\mathrm{ct}}^{\mathrm{FF}}(r_{\mathrm{full}}) - \sum_{F} U_{\mathrm{ct}}^{\mathrm{FF}}(r_{\mathrm{F}}). \tag{S37}$$

And the fitting target of $U_{\mathrm{ct}}^{\mathrm{FF,inter}}$ is $U_{\mathrm{ct}}^{\mathrm{EDA}}$ as defined in Eq. S25.

Besides, the total interaction energy, $U_{\mathrm{total}}^{\mathrm{FF,inter}}$ is the sum of all the decomposed interaction energies:

$$\begin{aligned} U_{\mathrm{total}}^{\mathrm{FF,inter}} &= U_{\mathrm{est\_rep}}^{\mathrm{FF,inter}} + U_{\mathrm{disp}}^{\mathrm{FF,inter}} + U_{\mathrm{pol}}^{\mathrm{FF,inter}} + U_{\mathrm{ct}}^{\mathrm{FF,inter}} && \text{(S38)} \\ &= U^{\mathrm{FF}}(r_{\mathrm{full}}) - \sum_{F} U^{\mathrm{FF}}(r_F). && \text{(S39)} \end{aligned}$$

Naturally, $U_{\mathrm{total}}^{\mathrm{FF,inter}}$ is fitted to $U_{\mathrm{int}}^{\mathrm{DFT}}$ as defined in Eq. S4.

The interaction energies were trained using a scaled mean squared error (SMSE) loss, defined as:

$$\mathcal{L}_{\mathrm{SMSE}}^{\mathrm{term}} = \frac{1}{N} \sum_{i} s_i^{\mathrm{Boltz}} s_i^{\mathrm{Force}} \left( U_{\mathrm{term},i}^{\mathrm{FF,inter}} - U_{\mathrm{term},i}^{\mathrm{EDA}} \right)^2, \tag{S40}$$

where the symbol "term" corresponds to specific interaction term, e.g., "disp", "est_rep", "pol" and "ct". Two scaling factors are applied to the squared deviation:

Similar to the approach in ByteFF,[19] the Boltzmann weight, $s_i^{\mathrm{Boltz}}$, downweights dimers with extremely large interaction energies (strong repulsion):

$$s_i^{\mathrm{Boltz}} = \min\left(1.0, \exp\left(\frac{\alpha - \min(U_{\mathrm{int}}^{\mathrm{DFT}}, U_{\mathrm{total}}^{\mathrm{FF,inter}})}{\beta}\right)\right). \tag{S41}$$

This factor is tuned by two hyperparameters, $\alpha$ and $\beta$, set to 10.0 and 2.0 kcal/mol respectively.

The second factor, $s_i^{\mathrm{Force}}$, reduces the importance of dimers with excessively large atomic

forces:

$$s_i^{\text{Force}}(F_{\max}) = \begin{cases} 1, & \text{if } x < F_{\text{lower}} \\ \frac{1}{2}\left(\cos\left(\frac{F_{\max}-F_{\text{lower}}}{F_{\text{upper}}-F_{\text{lower}}}\cdot\pi\right)+1\right), & \text{if } F_{\text{lower}} \le x < F_{\text{upper}} \\ 0, & \text{if } x \ge F_{\text{upper}} \end{cases} \tag{S42}$$

Here, $F_{\max}$ denotes the maximum magnitude of atomic forces in the dimer. Since we do not have the QM atomic force, they are approximated using force field predictions. And this factor is tuned by two hyperparameters, $F_{\text{lower}}$ and $F_{\text{upper}}$, set to 50.0 and 80.0 kcal/mol/Å, respectively.

Finally, the total loss is written as:

$$\mathcal{L}_{\text{train}} = w_{\text{total}}\mathcal{L}_{\text{SMSE}}^{\text{total}} + w_{\text{pol}}\mathcal{L}_{\text{SMSE}}^{\text{pol}} + w_{\text{disp}}\mathcal{L}_{\text{SMSE}}^{\text{disp}} + w_{\text{ct}}\mathcal{L}_{\text{SMSE}}^{\text{ct}} + w_{\text{est\_rep}}\mathcal{L}_{\text{SMSE}}^{\text{est\_rep}}, \tag{S43}$$

where $w_{\text{total}}$ is set to 10.0 and the other weights are set to 1.0. During training, all model parameters except those corresponding to non-bonded parameters in the output layer were frozen; consequently, the atomic hidden representations and bonded parameters remained unchanged.

## 7.3 Fine-tuning Stage

The bonded parameters of ByteFF were trained with the GAFF2[20] non-bonded parameters. Given that torsion parameters are strongly coupled to non-bonded interactions, the torsion parameters predicted by ByteFF are incompatible with ByteFF-Pol, which features newly designed and trained non-bonded interactions. Therefore, we further fine-tuned the torsion parameters in the final stage. For this fine-tuning of ByteFF-Pol's torsion parameters, we utilized the same torsion scan data employed in ByteFF training, combined with the BMSE loss. During training, all model parameters except those corresponding to torsion parameters in the output layer were frozen, ensuring that the non-bonded interactions and other bonded

parameters remained unchanged.

# 8 Simulation Details

The macroscopic properties including density ($\rho$), evaporation enthalpy ($\Delta H_{\text{vap}}$), viscosity ($\eta$) and conductivity ($\sigma$) were computed from the MD simulations. These simulations were executed using the OpenMM software package[21] on L20 GPU cards. Different force field including OPLS-AA, OpenFF and ByteFF-Pol were simulated under the same protocols as described bellow. To enhance computational efficiency, the r-RESPA multiple time step Langevin integrator[22] was employed for most simulations, with a time step of 2 fs for non-bonded interactions and 1 fs for bonded interactions, unless otherwise specified. For the evaluation of density and evaporation enthalpy, we constructed simulation systems containing approximately 5,000 atoms, corresponding to the experimental components; for other properties, simulation systems with around 10,000 atoms were employed.

## 8.1 Density

To evaluate density, we performed 3 ns MD simulations using a Monte Carlo barostat at 1 bar and temperatures corresponding to the experimental conditions in the $NpT$ ensemble, with thermodynamic properties recorded every 1 ps. The mean and standard deviation of the densities were then computed via bootstrapping using values from the final 1 ns of the simulations.

## 8.2 Evaporation Enthalpy

For evaporation enthalpy, the liquid and gas phases were simulated separately.[23] The MD simulation protocol used for the liquid phase was identical to that employed for density evaluation. The average potential energy of the liquid phase, $\langle U_{\text{liquid}} \rangle$, was obtained via bootstrapping, utilizing potential energy values from the final 1 ns of the simulations.

The gas phase was modeled under the assumption of ideal gas behavior. For each simulation, a single isolated molecule was simulated without periodic boundary conditions (PBC).

MD simulations of 0.3 ns were performed in the $NVT$ ensemble, with a time step of 0.2 fs for non-bonded interactions and 0.1 fs for bonded interactions. Thermodynamic properties were recorded at 0.1 ps intervals. The average potential energy of the gas phase, $\langle U_{\text{gas}} \rangle$, was determined via bootstrapping using potential energy values from the final 0.1 ns of the simulations.

Finally, the evaporation enthalpy was computed as:

$$\Delta H_{\text{vap}} = \langle U_{\text{gas}} \rangle - \langle U_{\text{liquid}} \rangle + p\Delta V \approx \langle U_{\text{gas}} \rangle - \langle U_{\text{liquid}} \rangle + RT. \tag{S44}$$

The $p\Delta V$ term accounts for the work of volume change during evaporation, approximated by the volume of ideal gas and ignore the volume of liquid phase.

## 8.3 Viscosity

The viscosity was evaluated using the periodic perturbation method,[24] which has demonstrated to be accurate and efficient for viscous liquids like electrolytes. In this method, an acceleration along the $x$ direction, with periodic in $z$, is applied in an otherwise normal $NpT$ simulation,

$$a_x(z) = A \cos\left(\frac{2\pi z}{l_z}\right), \tag{S45}$$

where $l_z$ is the $z$-length of the simulation box. In the steady state, the acceleration will generate a velocity gradient,

$$v_x(z) = W \cos\left(\frac{2\pi z}{l_z}\right). \tag{S46}$$

The velocity amplitude $W$ is calculated by ensemble averaging of the simulation data. Through Stokes' equation, the amplitude is related to the viscosity $\eta$ by

$$W = \frac{A\rho}{\eta}\left(\frac{l_z}{2\pi}\right)^2. \tag{S47}$$

This method was implemented as an OpenMM plugin by Dr. Gong.[25]

After 4 ns $NpT$ and subsequently 2 ns $NVT$ relaxation, 1 ns perturbation simulation were conducted with $A = 0.02\text{nm/ps}^2$ and 1 fs time step for both bonded and non-bonded interactions. The velocity amplitude $W$ was recorded at 0.5 ps intervals, and viscosity was calculated as:

$$\eta = \frac{1}{\langle \frac{W}{A\rho} \left(\frac{2\pi}{l_z}\right)^2 \rangle}. \tag{S48}$$

The final viscosity value and its standard deviation were computed from results of four parallel simulations.

## 8.4 Conductivity

The conductivity was computed from the Onsager transport coefficients. For a system containing molecular species $i$ and $j$ with $N_i$ and $N_j$ molecules, respectively, we define the correlation function

$$C_{ij}(t) = \left\langle \sum_{k=1}^{N_i} [\boldsymbol{r}_{ik}(t) - \boldsymbol{r}_{ik}(0)] \cdot \sum_{l=1}^{N_j} [\boldsymbol{r}_{jl}(t) - \boldsymbol{r}_{jl}(0)] \right\rangle, \tag{S49}$$

where $\boldsymbol{r}$ is the center of mass of each molecule in the barycentric reference frame, and $\langle \cdots \rangle$ denotes an average over arbitrary time origins. The Onsager transport coefficients[26] are then

$$\Lambda_{ij} = \frac{1}{6N} \frac{\partial}{\partial t} \lim_{t \to \infty} C_{ij}(t), \tag{S50}$$

or, equivalently,[27]

$$L_{ij} = \frac{\beta}{6V} \frac{\partial}{\partial t} \lim_{t \to \infty} C_{ij}(t), \tag{S51}$$

where $N$ is the total number of molecules, $\beta = 1/(k_\text{B}T)$, and $V$ is the system volume. Let $z_i$ be the signed integer charge of species $i$, and let $e$ be the elementary charge. The ionic conductivity[27] $\sigma$ is

$$\sigma = e^2 \sum_{ij} z_i z_j L_{ij}. \tag{S52}$$

For each simulation system, we first conducted 8 ns $NpT$ simulations, which was chosen to be long enough to relax the solvation structure of the lithium ions. Subsequently, 20 ns $NVT$ simulations were performed to generate the MD trajectories, saved every 1 ps. The Onsager transport coefficients $L_{ij}$ were obtained directly from Eq. S51 by fitting the slope of $C_{ij}(t)$ between 50 and 200 ps (the interval where $C_{ij}(t)$ is approximately linear). Equation S51 has the form of an Einstein relation between the transport coefficient $L_{ij}$ and the mean-"squared" displacement given by $\sum_{k=1}^{N_i} \boldsymbol{r}_{ik}(t)$ and $\sum_{l=1}^{N_j} \boldsymbol{r}_{jl}(t)$. A corresponding Green-Kubo relation also exists; we therefore examined the velocity correlation function (VCF) of $\sum_{k=1}^{N_i} \dot{\boldsymbol{r}}_{ik}(t)$ and $\sum_{l=1}^{N_j} \dot{\boldsymbol{r}}_{jl}(t)$ to ensure that the fitting window is comparable to the time scale over which the VCF decays to zero. Similar to viscosity, the final conductivity value and its standard deviation were computed from results of four parallel simulations.

## 8.5 Self-Diffusion Coefficient

Self-diffusion coefficient ($D_i$) for species $i$ is evaluated using the Einstein formula:

$$\begin{aligned} D_i &= \frac{1}{6}\frac{\mathrm{d}}{\mathrm{d}t}\lim_{t\to\infty}\langle \mathrm{MSD}(t)\rangle \\ &= \frac{1}{6}\frac{\mathrm{d}}{\mathrm{d}t}\lim_{t\to\infty}\langle |\boldsymbol{r}(t+t_0)-\boldsymbol{r}(t_0)|^2\rangle, \end{aligned} \tag{S53}$$

where MSD is the mean-square displacement of a molecule (of species $i$) center-of-mass, and the ensemble average is realized by averaging over different time origins $t_0$ and all the molecules of species $i$.

In practice, the simulation system was first relaxed by a 4 ns $NpT$ simulation. Subsequently, 2 ns $NVT$ simulation was performed to collect the MD trajectories, saved every 1 ps. Similarly, the final self-diffusion coefficient value and its standard deviation were computed from results of four parallel simulations.

## 8.6 Path-Integral Molecular Dynamics

We performed path-integral molecular dynamics (PIMD) simulations[28] to address the nuclear quantum effect (NQE). The "RPMDIntegrator" and "RPMDMonteCarloBarostat" implemented in OpenMM[21] were used for the $NpT$ ensemble simulations, with 16 copies of the system.

The MD protocol for evaluating density and evaporation enthalpy is similar to that described for classical MD simulations. Key differences include: for the liquid phase, a smaller time step (0.5 fs) was employed due to the inherent large energy fluctuations in PIMD; for the gas phase, the simulation time was extended to 2 ns, with the final 0.8 ns used for potential energy evaluation.

Eq. S44 is also used to compute the evaporation enthalpy for the PIMD simulations. It should be noted that this method introduces a further approximation for systems including NQE, as the kinetic energies of the gas and liquid phases may not perfectly cancel each other.

# 9 Comparison with Other Force Fields

We compare the performance of ByteFF-Pol with other force fields involving electrolyte systems, including APPLE&P,[1] QRNN[3] and BAMBOO.[2]

Table S2: Comparison of density predictions between ByteFF-Pol ($\rho_{\mathrm{ByteFF-Pol}}$) and APPLE&P ($\rho_{\mathrm{APPLE\&P}}$).[1] The components of each simulation system is provided as the molecular ratio and abbreviations. The source of the experimental data can be found in Ref 2 Tab S6.

| System | $T$ [K] | $\rho_{\mathrm{exp}}$ [g/mL] | $\rho_{\mathrm{APPLE\&P}}$ [g/mL] | $\rho_{\mathrm{ByteFF-Pol}}$ [g/mL] |
|---|---|---|---|---|
| 1DMC | 298 | 1.06 | 1.040 | 1.079 |
| 1EC | 313 | 1.32 | 1.302 | 1.319 |
| 1PC | 298 | 1.20 | 1.209 | 1.203 |

Table S3: Comparison of conductivity predictions between ByteFF-Pol ($\sigma_{\mathrm{ByteFF-Pol}}$) and APPLE&P ($\sigma_{\mathrm{APPLE\&P}}$).[1] The components of each simulation system is provided as the molecular ratio and abbreviations. The source of the experimental data can be found in Ref 2 Tab S6.

| System | $T$ [K] | $\sigma_{\mathrm{exp}}$ [mS/cm] | $\sigma_{\mathrm{APPLE\&P}}$ [mS/cm] | $\sigma_{\mathrm{ByteFF-Pol}}$ [mS/cm] |
|---|---|---|---|---|
| 13EC-13DMC-2LiPF6 | 298 | 12.0 | 13.5 | 12.815 |
| 13EC-13DMC-2LiTFSI | 298 | 9.0 | 12 | 10.431 |
| 10EC-10DMC-2LiPF6 | 298 | 11.7 | 15.9 | 13.501 |
| 10EC-10DMC-2LiPF6 | 333 | 19.5 | 25.9 | 23.143 |

Table S4: Comparison of density predictions between ByteFF-Pol ($\rho_{\mathrm{ByteFF-Pol}}$) and QRNN ($\rho_{\mathrm{QRNN}}$).[3] The components of each simulation system is provided as the molecular ratio and abbreviations. The source of the experimental data can be found in Ref 3 Tab S7.

| System | $T$ [K] | $\rho_{\mathrm{exp}}$ [g/mL] | $\rho_{\mathrm{QRNN}}$ [g/mL] | $\rho_{\mathrm{ByteFF-Pol}}$ [g/mL] |
|---|---|---|---|---|
| 1DMC | 298 | 1.06 | 1.0 | 1.079 |
| 1EC | 313 | 1.32 | 1.35 | 1.319 |
| 1PC | 298 | 1.2 | 1.22 | 1.203 |
| 1EMC | 298 | 1.0 | 0.99 | 1.027 |
| 1DEC | 298 | 0.97 | 0.92 | 0.991 |
| 1VC | 298 | 1.355 | 1.31 | 1.376 |
| 1FEC | 313 | 1.477 | 1.47 | 1.493 |

Table S5: Comparison of viscosity predictions between ByteFF-Pol ($\mu_{\mathrm{ByteFF-Pol}}$) and QRNN ($\mu_{\mathrm{QRNN}}$).[3] The components of each simulation system is provided as the molecular ratio and abbreviations. The source of the experimental data can be found in Ref 3 Tab S7.

| System | $T$ [K] | $\mu_{\mathrm{exp}}$ [cP] | $\mu_{\mathrm{QRNN}}$ [cP] | $\mu_{\mathrm{ByteFF-Pol}}$ [cP] |
|---|---|---|---|---|
| 1DMC | 298 | 0.585 | 0.79 | 0.689 |
| 1EC | 313 | 1.93 | 2.27 | 1.662 |
| 1PC | 298 | 2.53 | 2.6 | 2.15 |
| 1EMC | 298 | 0.65 | 0.65 | 0.817 |
| 1DEC | 298 | 0.749 | 0.43 | 0.986 |
| 1VC | 298 | 1.78 | 1.26 | 1.556 |
| 1FEC | 313 | 3.17 | 3.02 | 2.916 |
| 46DMC-20EC | 313 | 0.73 | 0.83 | 0.8 |
| 46DMC-20EC-3LiPF6 | 313 | 1.18 | 1.65 | 1.331 |
| 46DMC-20EC-6LiPF6 | 313 | 1.92 | 2.02 | 2.159 |
| 46DMC-20EC-9LiPF6 | 313 | 3.21 | 6.98 | 3.881 |
| 46DMC-20EC-12LiPF6 | 313 | 5.1 | 22.38 | 7.14 |

Table S6: Overall comparison between ByteFF-Pol and BAMBOO[2] for electrolyte properties.

| | | Density | | |
|---|---|---|---|---|
| | $n_{\text{system}}$ | MAE (g/mL) | MAPE | Pearson |
| BAMBOO | 45 | 0.018 | 1.60% | 0.99 |
| ByteFF-Pol | 45 | 0.027 | 2.23% | 0.99 |
| | | Viscosity | | |
| | $n_{\text{system}}$ | MAE (cP) | MAPE | Pearson |
| BAMBOO | 46 | 1.019 | 23.58% | 0.96 |
| ByteFF-Pol | 46 | 1.295 | 22.70% | 0.96 |
| | | Conductivity | | |
| | $n_{\text{system}}$ | MAE (mS/cm) | MAPE | Pearson |
| BAMBOO | 34 | 2.470 | 24.32% | 0.82 |
| ByteFF-Pol | 34 | 1.057 | 11.51% | 0.93 |

Table S7: Comparison of density predictions between ByteFF-Pol ($\rho_{\mathrm{ByteFF-Pol}}$) and BAMBOO ($\rho_{\mathrm{BAMBOO}}$).[2] The components of each simulation system is provided as the molecular ratio and abbreviations. The source of the experimental data can be found in Ref 2.

| System | $T$ [K] | $\rho_{\mathrm{exp}}$ [g/mL] | $\rho_{\mathrm{BAMBOO}}$ [g/mL] | $\rho_{\mathrm{ByteFF-Pol}}$ [g/mL] | Source |
|---|---|---|---|---|---|
| 1DMC | 298 | 1.06 | 1.06 | 1.079 | Tab S7[2] |
| 1EC | 313 | 1.32 | 1.31 | 1.319 | Tab S7[2] |
| 1PC | 298 | 1.2 | 1.188 | 1.203 | Tab S7[2] |
| 1EMC | 298 | 1.0 | 1.015 | 1.027 | Tab S7[2] |
| 1DEC | 298 | 0.97 | 0.969 | 0.991 | Tab S7[2] |
| 1VC | 298 | 1.355 | 1.37 | 1.376 | Tab S7[2] |
| 1FEC | 313 | 1.477 | 1.474 | 1.493 | Tab S7[2] |
| 1MA | 298 | 0.938 | 1.02 | 0.953 | Tab S11[2] |
| 1MP | 298 | 0.915 | 0.984 | 0.937 | Tab S11[2] |
| 1EF | 298 | 0.922 | 0.924 | 0.927 | Tab S11[2] |
| 1EIB | 298 | 0.865 | 0.829 | 0.889 | Tab S11[2] |
| 1ACAN | 298 | 1.08 | 1.014 | 1.104 | Tab S11[2] |
| 1DOX | 298 | 1.03 | 1.021 | 1.043 | Tab S11[2] |
| 1H6ZE | 298 | 1.413 | 1.488 | 1.554 | Tab S11[2] |
| 1FM47 | 298 | 1.601 | 1.571 | 1.687 | Tab S11[2] |
| 1N64 | 298 | 1.6 | 1.67 | 1.652 | Tab S11[2] |
| 1DMC | 298 | 1.06 | 1.06 | 1.079 | Tab S12[2] |
| 1DEC | 298 | 0.97 | 0.969 | 0.991 | Tab S12[2] |
| 1PC | 298 | 1.2 | 1.188 | 1.203 | Tab S12[2] |
| 1EC | 313 | 1.32 | 1.31 | 1.319 | Tab S12[2] |
| 1FEC | 313 | 1.477 | 1.474 | 1.493 | Tab S12[2] |
| 1EA | 298 | 0.9 | 0.892 | 0.922 | Tab S12[2] |
| 1NOV | 298 | 1.41 | 1.416 | 1.496 | Tab S12[2] |
| 249DMC-170EC-34LiPF6 | 298 | 1.239 | 1.236 | 1.279 | Tab S12[2] |
| 170EC-153DMC-15EMC-34LiPF6 | 298 | 1.273 | 1.274 | 1.318 | Tab S12[2] |
| 388DMC-170EC-75LiPF6 | 298 | 1.268 | 1.255 | 1.314 | Tab S12[2] |
| 5DMC-1LiFSI | 298 | 1.27 | 1.26 | 1.299 | Tab S12[2] |
| 23EC-1LiFSI | 298 | 1.38 | 1.359 | 1.386 | Tab S12[2] |
| 10EC-1LiFSI | 298 | 1.43 | 1.412 | 1.44 | Tab S12[2] |
| 1EMC | 298 | 1.0 | 1.015 | 1.027 | Tab S13[2] |
| 1VC | 298 | 1.355 | 1.37 | 1.376 | Tab S13[2] |
| 1EO | 298 | 0.79 | 0.769 | 0.834 | Tab S13[2] |
| 1ACT | 298 | 0.79 | 0.808 | 0.79 | Tab S13[2] |
| 1EP | 298 | 0.884 | 0.919 | 0.911 | Tab S13[2] |
| 170EC-166DMC-15LiPF6 | 298 | 1.235 | 1.224 | 1.259 | Tab S13[2] |
| 388DMC-170EC-50LiPF6 | 298 | 1.228 | 1.221 | 1.265 | Tab S13[2] |
| 388DMC-170EC-65LiPF6 | 298 | 1.252 | 1.243 | 1.295 | Tab S13[2] |
| 3DMC-1LiFSI | 298 | 1.36 | 1.361 | 1.388 | Tab S13[2] |
| 10DMC-1LiFSI | 298 | 1.18 | 1.167 | 1.205 | Tab S13[2] |
| 3EC-1LiFSI | 298 | 1.57 | 1.555 | 1.598 | Tab S13[2] |
| 5EC-1LiFSI | 298 | 1.5 | 1.484 | 1.522 | Tab S13[2] |
| 3EC-3DMC-2LiFSI | 298 | 1.46 | 1.456 | 1.484 | Tab S13[2] |
| 5EC-5DMC-2LiFSI | 298 | 1.38 | 1.372 | 1.399 | Tab S13[2] |
| 10EC-10DMC-2LiFSI | 298 | 1.3 | 1.285 | 1.313 | Tab S13[2] |
| 23EC-23DMC-2LiFSI | 298 | 1.24 | 1.229 | 1.253 | Tab S13[2] |

Table S8: Comparison of viscosity predictions between ByteFF-Pol ($\eta_{\mathrm{ByteFF-Pol}}$) and BAMBOO ($\eta_{\mathrm{BAMBOO}}$).[2] The components of each simulation system is provided as the molecular ratio and abbreviations. The source of the experimental data can be found in Ref 2.

| System | $T$ [K] | $\eta_{\mathrm{exp}}$ [cP] | $\eta_{\mathrm{BAMBOO}}$ [cP] | $\eta_{\mathrm{ByteFF-Pol}}$ [cP] | Source |
|---|---|---|---|---|---|
| 1DMC | 298 | 0.585 | 0.629 | 0.689 | Tab S7[2] |
| 1EC | 313 | 1.93 | 1.381 | 1.662 | Tab S7[2] |
| 1PC | 298 | 2.53 | 1.426 | 2.15 | Tab S7[2] |
| 1EMC | 298 | 0.65 | 0.724 | 0.817 | Tab S7[2] |
| 1DEC | 298 | 0.749 | 0.766 | 0.986 | Tab S7[2] |
| 1VC | 298 | 1.78 | 1.104 | 1.556 | Tab S7[2] |
| 1FEC | 313 | 3.17 | 2.349 | 2.916 | Tab S7[2] |
| 46DMC-20EC | 313 | 0.73 | 0.756 | 0.8 | Tab S7[2] |
| 46DMC-20EC-3LiPF6 | 313 | 1.18 | 1.448 | 1.331 | Tab S7[2] |
| 46DMC-20EC-6LiPF6 | 313 | 1.92 | 2.398 | 2.159 | Tab S7[2] |
| 46DMC-20EC-9LiPF6 | 313 | 3.21 | 4.328 | 3.881 | Tab S7[2] |
| 46DMC-20EC-12LiPF6 | 313 | 5.1 | 6.351 | 7.14 | Tab S7[2] |
| 1MA | 298 | 0.385 | 0.831 | 0.417 | Tab S11[2] |
| 1EF | 298 | 0.49 | 0.649 | 0.378 | Tab S11[2] |
| 1EIB | 298 | 0.56 | 0.524 | 0.719 | Tab S11[2] |
| 1ACAN | 298 | 0.85 | 0.88 | 1.079 | Tab S11[2] |
| 1DOX | 298 | 1.2 | 0.673 | 1.218 | Tab S11[2] |
| 1N64 | 298 | 0.64 | 1.381 | 1.058 | Tab S11[2] |
| 1DMC | 298 | 0.585 | 0.629 | 0.689 | Tab S12[2] |
| 1DEC | 298 | 0.749 | 0.766 | 0.986 | Tab S12[2] |
| 1PC | 298 | 2.53 | 1.426 | 2.15 | Tab S12[2] |
| 1EC | 313 | 1.93 | 1.381 | 1.662 | Tab S12[2] |
| 1FEC | 313 | 3.17 | 2.349 | 2.916 | Tab S12[2] |
| 1EA | 298 | 0.43 | 0.542 | 0.515 | Tab S12[2] |
| 1NOV | 298 | 0.45 | 0.447 | 0.744 | Tab S12[2] |
| 1EMC | 298 | 0.65 | 0.724 | 0.817 | Tab S13[2] |
| 1VC | 298 | 1.78 | 1.104 | 1.556 | Tab S13[2] |
| 1EO | 298 | 1.1 | 0.829 | 1.46 | Tab S13[2] |
| 1ACT | 298 | 0.31 | 0.502 | 0.284 | Tab S13[2] |
| 1EP | 298 | 0.631 | 0.728 | 0.611 | Tab S13[2] |
| 170EC-166DMC-15LiPF6 | 298 | 2.219 | 1.891 | 2.093 | Tab S15[2] |
| 388DMC-170EC-50LiPF6 | 298 | 2.734 | 2.683 | 3.023 | Tab S15[2] |
| 249DMC-170EC-34LiPF6 | 298 | 2.778 | 2.847 | 3.013 | Tab S15[2] |
| 170EC-153DMC-15EMC-34LiPF6 | 298 | 4.566 | 4.716 | 4.45 | Tab S15[2] |
| 388DMC-170EC-75LiPF6 | 298 | 4.472 | 4.81 | 5.332 | Tab S15[2] |
| 388DMC-170EC-65LiPF6 | 298 | 3.767 | 3.984 | 4.371 | Tab S15[2] |
| 10EC-10DMC-2LiFSI | 298 | 3.4 | 3.548 | 3.683 | Tab S15[2] |
| 5EC-5DMC-2LiFSI | 298 | 9.8 | 11.121 | 12.911 | Tab S15[2] |
| 3EC-3DMC-2LiFSI | 298 | 36.9 | 24.946 | 66.213 | Tab S15[2] |
| 5DMC-1LiFSI | 298 | 3.9 | 4.653 | 7.501 | Tab S15[2] |
| 23EC-1LiFSI | 298 | 4.1 | 3.184 | 3.711 | Tab S15[2] |
| 10EC-1LiFSI | 298 | 8.1 | 6.179 | 7.882 | Tab S15[2] |
| 3DMC-1LiFSI | 298 | 12.9 | 13.304 | 22.893 | Tab S15[2] |
| 10DMC-1LiFSI | 298 | 1.5 | 1.629 | 2.139 | Tab S15[2] |
| 5EC-1LiFSI | 298 | 33.1 | 17.283 | 34.597 | Tab S15[2] |
| 23EC-23DMC-2LiFSI | 298 | 1.9 | 1.85 | 1.999 | Tab S15[2] |

Table S9: Comparison of conductivity predictions between ByteFF-Pol ($\sigma_{\mathrm{ByteFF-Pol}}$) and BAMBOO ($\sigma_{\mathrm{BAMBOO}}$).[2] The components of each simulation system is provided as the molecular ratio and abbreviations. The source of the experimental data can be found in Ref 2.

| System | $T$ [K] | $\sigma_{\mathrm{exp}}$ [mS/cm] | $\sigma_{\mathrm{BAMBOO}}$ [mS/cm] | $\sigma_{\mathrm{ByteFF-Pol}}$ [mS/cm] | Source |
|---|---|---|---|---|---|
| 13EC-13DMC-2LiPF6 | 298 | 12.0 | 11.74 | 12.815 | Tab S6[2] |
| 13EC-13DMC-2LiTFSI | 298 | 9.0 | 6.359 | 10.431 | Tab S6[2] |
| 10EC-10DMC-2LiPF6 | 298 | 11.7 | 10.269 | 13.501 | Tab S6[2] |
| 10EC-10DMC-2LiPF6 | 333 | 19.5 | 20.49 | 23.143 | Tab S6[2] |
| 74PC-9EC-9DMC-8LiPF6 | 298 | 7.63 | 4.04 | 8.375 | Tab S9[2] |
| 65DMC-14EC-12PC-8LiPF6 | 298 | 13.41 | 10.87 | 12.591 | Tab S9[2] |
| 69DMC-17EC-6PC-8LiPF6 | 298 | 13.62 | 6.47 | 13.23 | Tab S9[2] |
| 37DMC-28PC-28EC-8LiPF6 | 298 | 11.52 | 11.67 | 10.654 | Tab S9[2] |
| 65DMC-18PC-8EC-8LiPF6 | 298 | 13.4 | 10.74 | 13.038 | Tab S9[2] |
| 65DMC-14EC-13PC-8LiPF6 | 298 | 13.41 | 11.6 | 12.622 | Tab S9[2] |
| 65DMC-20EC-6PC-8LiPF6 | 298 | 13.69 | 11.64 | 12.607 | Tab S9[2] |
| 46EC-37DMC-9PC-8LiPF6 | 298 | 11.62 | 7.46 | 12.644 | Tab S9[2] |
| 65DMC-25PC-3EC-8LiPF6 | 298 | 12.65 | 9.99 | 12.577 | Tab S9[2] |
| 65DMC-17PC-9EC-8LiPF6 | 298 | 13.4 | 10.06 | 12.115 | Tab S9[2] |
| 170EC-166DMC-15LiPF6 | 298 | 12.142 | 11.201 | 11.928 | Tab S15[2] |
| 388DMC-170EC-25LiPF6 | 298 | 10.89 | 11.361 | 11.323 | Tab S15[2] |
| 388DMC-170EC-42LiPF6 | 298 | 12.905 | 11.99 | 12.723 | Tab S15[2] |
| 388DMC-170EC-50LiPF6 | 298 | 12.427 | 12.881 | 14.204 | Tab S15[2] |
| 249DMC-170EC-34LiPF6 | 298 | 12.793 | 11.531 | 11.922 | Tab S15[2] |
| 170EC-153DMC-15EMC-34LiPF6 | 298 | 12.175 | 8.021 | 12.683 | Tab S15[2] |
| 388DMC-170EC-75LiPF6 | 298 | 12.144 | 8.713 | 12.172 | Tab S15[2] |
| 388DMC-170EC-65LiPF6 | 298 | 12.118 | 9.573 | 12.193 | Tab S15[2] |
| 276PC-52LiPF6 | 298 | 4.967 | 4.735 | 2.613 | Tab S15[2] |
| 10EC-10DMC-2LiFSI | 298 | 14.0 | 9.828 | 13.969 | Tab S15[2] |
| 5EC-5DMC-2LiFSI | 298 | 9.8 | 4.369 | 8.669 | Tab S15[2] |
| 3EC-3DMC-2LiFSI | 298 | 4.5 | 2.266 | 3.419 | Tab S15[2] |
| 5DMC-1LiFSI | 298 | 12.2 | 9.237 | 10.353 | Tab S15[2] |
| 23EC-1LiFSI | 298 | 8.7 | 7.013 | 9.084 | Tab S15[2] |
| 10EC-1LiFSI | 298 | 9.7 | 5.907 | 9.509 | Tab S15[2] |
| 3DMC-1LiFSI | 298 | 8.1 | 4.363 | 5.19 | Tab S15[2] |
| 10DMC-1LiFSI | 298 | 9.9 | 15.984 | 14.914 | Tab S15[2] |
| 3EC-1LiFSI | 298 | 2.3 | 1.738 | 1.603 | Tab S15[2] |
| 5EC-1LiFSI | 298 | 5.6 | 2.597 | 4.669 | Tab S15[2] |
| 23EC-23DMC-2LiFSI | 298 | 11.5 | 11.015 | 11.641 | Tab S15[2] |

# References


(1) Borodin, O. Polarizable Force Field Development and Molecular Dynamics Simulations of Ionic Liquids. *The Journal of Physical Chemistry B* **2009**, *113*, 11463–11478, DOI: 10.1021/jp905220k.

(2) Gong, S.; Zhang, Y.; Mu, Z.; Pu, Z.; Wang, H.; Han, X.; Yu, Z.; Chen, M.; Zheng, T.; Wang, Z.; others A predictive machine learning force-field framework for liquid electrolyte development. *Nature Machine Intelligence* **2025**, 1–10.

(3) Dajnowicz, S.; Agarwal, G.; Stevenson, J. M.; Jacobson, L. D.; Ramezanghorbani, F.; Leswing, K.; Friesner, R. A.; Halls, M. D.; Abel, R. High-Dimensional Neural Network Potential for Liquid Electrolyte Simulations. *The Journal of Physical Chemistry B* **2022**, *126*, 6271–6280, DOI: 10.1021/acs.jpcb.2c03746, PMID: 35972463.

(4) Schrödinger, LLC Maestro. 2025; Schrödinger Release 2025-3.

(5) Chirico, R. D.; Frenkel, M.; Diky, V. V.; Marsh, K. N.; Wilhoit, R. C. ThermoML an XML-based approach for storage and exchange of experimental and critically evaluated thermophysical and thermochemical property data. 2. Uncertainties. *Journal of Chemical & Engineering Data* **2003**, *48*, 1344–1359.

(6) Yang, Z.; Wu, Y.; Han, X.; Zhang, Z.; Lai, H.; Mu, Z.; Zheng, T.; Liu, S.; Pu, Z.; Wang, Z.; others A Unified Predictive and Generative Solution for Liquid Electrolyte Formulation. *arXiv preprint arXiv:2504.18728* **2025**,

(7) Lide, D. R. *CRC Handbook of Chemistry and Physics*; CRC Press: Boca Raton, FL, 2004; Vol. 85.

(8) Wang, L.-P.; Song, C. Geometry optimization made simple with translation and rotation coordinates. *The Journal of Chemical Physics* **2016**, *144*, 214108, DOI: 10.1063/1.4952956.

(9) Epifanovsky, E. et al. Software for the Frontiers of Quantum Chemistry: An Overview of Developments in the Q-Chem 5 Package. *The Journal of Chemical Physics* **2021**, *155*, 084801, DOI: 10.1063/5.0055522.

(10) Khaliullin, R. Z.; Cobar, E. A.; Lochan, R. C.; Bell, A. T.; Head-Gordon, M. Unravelling the Origin of Intermolecular Interactions Using Absolutely Localized Molecular Orbitals. *The Journal of Physical Chemistry A* **2007**, *111*, 8753–8765, DOI: 10.1021/jp073685z.

(11) Horn, P. R.; Mao, Y.; Head-Gordon, M. Defining the contributions of permanent electrostatics, Pauli repulsion, and dispersion in density functional theory calculations of intermolecular interaction energies. *The Journal of Chemical Physics* **2016**, *144*, 114107, DOI: 10.1063/1.4942921.

(12) Horn, P. R.; Head-Gordon, M. Alternative definitions of the frozen energy in energy decomposition analysis of density functional theory calculations. *The Journal of Chemical Physics* **2016**, *144*, 084118, DOI: 10.1063/1.4941849.

(13) Horn, P. R.; Mao, Y.; Head-Gordon, M. Probing non-covalent interactions with a second generation energy decomposition analysis using absolutely localized molecular orbitals. *Physical Chemistry Chemical Physics* **2016**, *18*, 23067–23079, DOI: 10.1039/C6CP03784D.

(14) Mao, Y.; Loipersberger, M.; Horn, P. R.; Das, A.; Demerdash, O.; Levine, D. S.; Prasad Veccham, S.; Head-Gordon, T.; Head-Gordon, M. From Intermolecular Interaction Energies and Observable Shifts to Component Contributions and Back Again: A Tale of Variational Energy Decomposition Analysis. *Annual Review of Physical Chemistry* **2021**, *72*, 641–666, DOI: https://doi.org/10.1146/annurev-physchem-090419-115149.

(15) Horn, P. R.; Head-Gordon, M. Polarization contributions to intermolecular interac-

tions revisited with fragment electric-field response functions. *The Journal of Chemical Physics* **2015**, *143*, 114111, DOI: 10.1063/1.4930534.

(16) Aldossary, A.; Shen, H.; Wang, Z.; Head-Gordon, M. Uncoupled fragment electric-field response functions: An accelerated model for the polarization energy in energy decomposition analysis of intermolecular interactions. *Chemical Physics Letters* **2025**, *862*, 141825, DOI: https://doi.org/10.1016/j.cplett.2024.141825.

(17) Demerdash, O.; Mao, Y.; Liu, T.; Head-Gordon, M.; Head-Gordon, T. Assessing Many-Body Contributions to Intermolecular Interactions of the AMOEBA Force Field Using Energy Decomposition Analysis of Electronic Structure Calculations. *The Journal of Chemical Physics* **2017**, *147*, 161721, DOI: 10.1063/1.4999905.

(18) Thole, B. T. Molecular polarizabilities calculated with a modified dipole interaction. *Chemical Physics* **1981**, *59*, 341–350.

(19) Zheng, T.; Wang, A.; Han, X.; Xia, Y.; Xu, X.; Zhan, J.; Liu, Y.; Chen, Y.; Wang, Z.; Wu, X.; others Data-driven parametrization of molecular mechanics force fields for expansive chemical space coverage. *Chemical Science* **2025**, *16*, 2730–2740.

(20) Wang, J.; Wolf, R. M.; Caldwell, J. W.; Kollman, P. A.; Case, D. A. Development and Testing of a General Amber Force Field. *Journal of Computational Chemistry* **2004**, *25*, 1157–1174, DOI: 10.1002/jcc.20035.

(21) Eastman, P.; Swails, J.; Chodera, J. D.; McGibbon, R. T.; Zhao, Y.; Beauchamp, K. A.; Wang, L.-P.; Simmonett, A. C.; Harrigan, M. P.; Stern, C. D.; others OpenMM 7: Rapid development of high performance algorithms for molecular dynamics. *PLoS computational biology* **2017**, *13*, e1005659.

(22) Zhou, R.; Berne, B. J. A new molecular dynamics method combining the reference system propagator algorithm with a fast multipole method for simulating proteins and other complex systems. *The Journal of chemical physics* **1995**, *103*, 9444–9459.

(23) Ren, P.; Ponder, J. W. Polarizable atomic multipole water model for molecular mechanics simulation. *The Journal of Physical Chemistry B* **2003**, *107*, 5933–5947.

(24) Hess, B. Determining the shear viscosity of model liquids from molecular dynamics simulations. *The Journal of Chemical Physics* **2002**, *116*, 209–217, DOI: 10.1063/1.1421362.

(25) Gong, Z.; Padua, A. A. H. Effect of side chain modifications in imidazolium ionic liquids on the properties of the electrical double layer at a molybdenum disulfide electrode. *The Journal of Chemical Physics* **2021**, *154*, 084504, DOI: 10.1063/5.0040172.

(26) Krishna, R.; van Baten, J. M. The Darken Relation for Multicomponent Diffusion in Liquid Mixtures of Linear Alkanes: An Investigation Using Molecular Dynamics (MD) Simulations. *Industrial & Engineering Chemistry Research* **2005**, *44*, 6939–6947, DOI: 10.1021/ie050146c.

(27) Fong, K. D.; Bergstrom, H. K.; McCloskey, B. D.; Mandadapu, K. K. Transport Phenomena in Electrolyte Solutions: Nonequilibrium Thermodynamics and Statistical Mechanics. *AIChE Journal* **2020**, *66*, e17091, DOI: 10.1002/aic.17091.

(28) Tuckerman, M. E.; Tuckerman, M. E. *Statistical Mechanics: Theory and Molecular Simulation*, second edition, second edition ed.; Oxford Graduate Texts; Oxford University Press: Oxford, New York, 2023.